LETTER

doi:10.1038/nature12941

An optical lattice clock with accuracy and stability at the 10^{-18} level

B. J. Bloom[1,2]*, T. L. Nicholson[1,2]*, J. R. Williams[1,2]†, S. L. Campbell[1,2], M. Bishof[1,2], X. Zhang[1,2], W. Zhang[1,2], S. L. Bromley[1,2] & J. Ye[1,2]

Progress in atomic, optical and quantum science[1,2] has led to rapid improvements in atomic clocks. At the same time, atomic clock research has helped to advance the frontiers of science, affecting both fundamental and applied research. The ability to control quantum states of individual atoms and photons is central to quantum information science and precision measurement, and optical clocks based on single ions have achieved the lowest systematic uncertainty of any frequency standard[3–5]. Although many-atom lattice clocks have shown advantages in measurement precision over trapped-ion clocks[6,7], their accuracy has remained 16 times worse[8–10]. Here we demonstrate a many-atom system that achieves an accuracy of 6.4×10^{-18}, which is not only better than a single-ion-based clock, but also reduces the required measurement time by two orders of magnitude. By systematically evaluating all known sources of uncertainty, including *in situ* monitoring of the blackbody radiation environment, we improve the accuracy of optical lattice clocks by a factor of 22. This single clock has simultaneously achieved the best known performance in the key characteristics necessary for consideration as a primary standard—stability and accuracy. More stable and accurate atomic clocks will benefit a wide range of fields, such as the realization and distribution of SI units[11], the search for time variation of fundamental constants[12], clock-based geodesy[13] and other precision tests of the fundamental laws of nature. This work also connects to the development of quantum sensors and many-body quantum state engineering[14] (such as spin squeezing) to advance measurement precision beyond the standard quantum limit.

Accuracy for the SI (International System of Units) second is currently defined by the caesium (Cs) primary standard. However, optical atomic clocks have now achieved a lower systematic uncertainty[3–5,8,12]. This systematic uncertainty will become accuracy once the SI second has been redefined. Neutral atom clocks with many ultracold atoms confined in magic-wavelength optical lattices[15] have the potential for much greater precision than ion clocks[7–9,16]. This potential has been realized only very recently owing to the improved frequency stability of optical local oscillators[14,17,18], resulting in a record single-clock instability of $3.1 \times 10^{-16}/\sqrt{\tau}$, where τ is the averaging time in seconds[6]. This result represents a gain by a factor of 10 in our clock stability, allowing for a factor-of-100 reduction in the averaging time that is required to reach a desired uncertainty[6]. Equivalent instability at one second has also been recently achieved with ytterbium (Yb) optical lattice clocks[7] and averaging for seven hours was demonstrated, down to about 2×10^{-18} for a single clock. We used this measurement precision to evaluate the important systematic effects that have limited optical lattice clocks, and we achieve a total systematic uncertainty in fractional frequency of 6.4×10^{-18}, which is a factor-of-22 improvement over the best published total uncertainties for optical lattice clocks[8–10].

Now that the clock systematic uncertainty has been fully evaluated, it is a frequency standard at which the statistical uncertainty matches the total systematic uncertainty within 3,000 s. Combining improved clock designs with this measurement precision has allowed us to overcome two main obstacles to achieve the reductions in uncertainty reported here. First, we must understand and overcome the atomic-interaction-induced frequency shifts inherent in many-particle clocks[19–21]. We have now determined this effect with 6×10^{-19} uncertainty. Second, we need to measure the thermal radiation environment of the lattice-trapped atoms accurately, because this causes the largest systematic clock shift, known as the blackbody radiation (BBR) Stark shift. Incomplete knowledge of the thermal radiation impinging upon the atoms has so far dominated lattice clock uncertainty. We demonstrate that a combination of accurate *in situ* temperature probes and a thermal enclosure surrounding the clock vacuum chamber allows us to achieve an overall BBR shift uncertainty of 4.1×10^{-18}. This progress was enabled by a precise measurement (performed at the Physikalisch-Technische Bundesanstalt) of the Sr polarizability[22], which governs the magnitude of the BBR shift. Furthermore, we compared two independent Sr clocks and they agree within their combined total uncertainty of 5.4×10^{-17} over a period of one month.

To demonstrate the improved performance of lattice clocks, we built two Sr clocks in JILA[6,23] (see the Methods Summary for details). Herein we refer to the first-generation JILA Sr clock as SrI and the newly constructed Sr clock as SrII. The recent improvement of low-thermal-noise optical oscillators allowed us to demonstrate the stability of both Sr clocks, reaching within a factor of 2 of the quantum projection noise limit for 2,000 atoms[6]. We constructed the SrII clock with the goal of reducing the atomic-interaction-related and BBR-related frequency uncertainties. Thus, SrII has an optical trap volume about 100 times larger than that of SrI to reduce the atomic density, along with *in situ* BBR probes in vacuum to measure the thermal environment of the atoms, achieving a total systematic uncertainty of 6.4×10^{-18}. The improvement of SrI, on the other hand, has been a modest factor of 2 over our previous result[8], now achieving a total systematic uncertainty of 5.3×10^{-17}.

A major practical concern is the speed with which these clocks reach agreement at their stated uncertainties. Hence, the low instability of these Sr clocks (3×10^{-18} at about 10,000 s), displayed as the Allan deviation of their frequency comparison in Fig. 1a, is critical for evaluating systematic effects in a robust manner. Figure 1b documents a comparison of the SrI and SrII clocks over a period of one month, showing that their measured disagreement of $\nu_{\mathrm{SrII}} - \nu_{\mathrm{SrI}} = -2.8 \times 10^{-17}$, with 2×10^{-18} statistical uncertainty, is within their combined systematic uncertainty of 5.4×10^{-17}. The Allan deviation and the binned intercomparison data showcase the stability and reproducibility of these clocks on both short and long timescales. This performance level is necessary for a rigorous evaluation of clock systematics at the 10^{-18} level.

SrI and SrII independently correct for systematic offsets to their measured atomic frequencies. Table 1 lists the major sources of frequency shifts Δ and their related uncertainties σ that affect both clocks. The SrI clock uncertainty is dominated by its BBR shift uncertainty of 4.5×10^{-17}.

[1]JILA, National Institute of Standards and Technology and University of Colorado, Boulder, Colorado 80309-0440, USA. [2]Department of Physics, University of Colorado, Boulder, Colorado 80309-0390, USA. †Present address: Jet Propulsion Laboratory, California Institute of Technology, Pasadena, California 91109, USA.
*These authors contributed equally to this work.

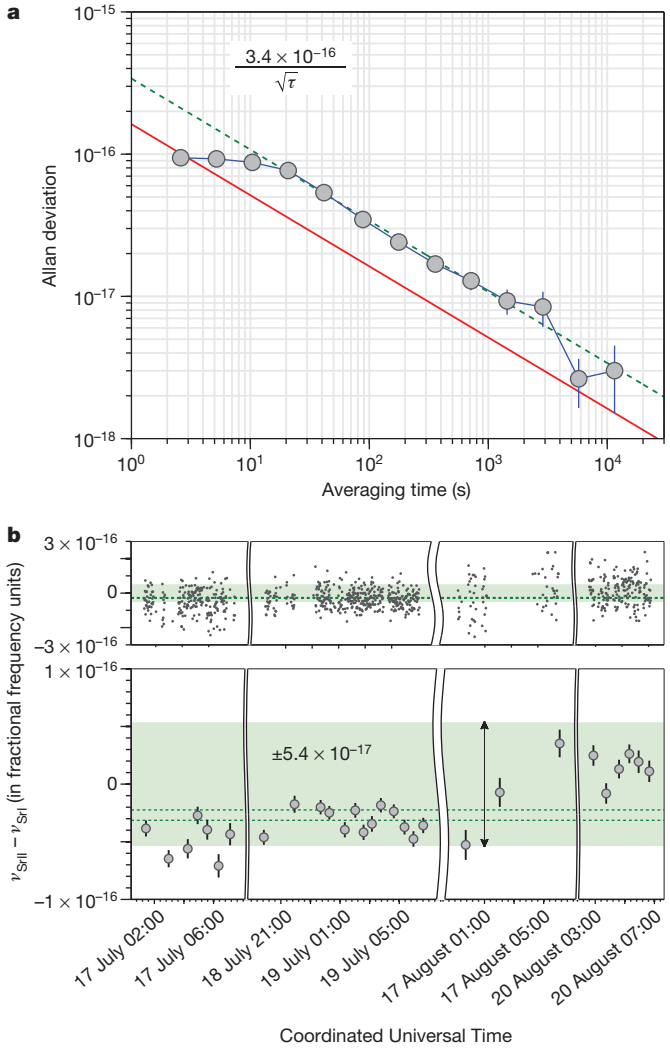

Figure 1 | Clock comparisons between SrI and SrII. a, Allan deviation of the SrI and SrII comparison divided by $\sqrt{2}$ to reflect the performance of a single clock. The red solid line is the calculated quantum projection noise for this comparison. The green dashed line is a fit to the data, showing the worst case scenario for the averaging of a single clock of 3.4×10^{-16} at one second. The vertical blue lines represent the 1σ standard errors for the Allan deviation. **b**, The absolute agreement between SrI and SrII recorded at the indicated Coordinated Universal Time. The light-green region denotes the 1σ combined systematic uncertainty for the two clocks under the running conditions at that time. The top panel shows the frequency record binned at 60 s; in the bottom panel each solid circle represents 30 min of averaged data. In the bottom panel, small solid black lines represent the 1σ standard errors inflated by the square root of the reduced chi-squared, $\sqrt{\chi^2_{\text{reduced}}}$. For clarity, we have omitted the error bars in the top panel. The green dashed lines represent the 1σ standard error inflated by the square root of the reduced chi-squared for the weighted mean of these binned comparison data. The final comparison over 52,000 s of data showed agreement at $-2.7(5)\times10^{-17}$ ($\sqrt{\chi^2_{\text{reduced}}}=10.5$) for the 30-min averaging time and $-2.8(2)\times10^{-17}$ ($\sqrt{\chi^2_{\text{reduced}}}=3.5$) for the 60-s averaging time (see Methods).

For SrII, on the other hand, all sources have been evaluated to produce uncertainties better than 4×10^{-18}.

The largest improvement (compared to other lattice clocks) in the total systematic uncertainty of SrII was obtained through control of the BBR shift. We enclosed the entire clock apparatus inside a BBR shielding box (Fig. 2a). Our lasers for cooling, trapping and clock spectroscopy are delivered to the inside of the BBR shielding box by optical fibres, preventing stray radiation from entering. We have also installed two

Table 1 | Frequency shifts and related uncertainties for SrI and SrII

Sources for shift	Δ_{SrI}	σ_{SrI}	Δ_{SrII}	σ_{SrII}
BBR static	−4,832	45	−4,962.9	1.8
BBR dynamic	−332	6	−345.7	3.7
Density shift	−84	12	−4.7	0.6
Lattice Stark	−279	11	−461.5	3.7
Probe beam a.c. Stark	8	4	0.8	1.3
First-order Zeeman	0	<0.1	−0.2	1.1
Second-order Zeeman	−175	1	−144.5	1.2
Residual lattice vector shift	0	<0.1	0	<0.1
Line pulling and tunnelling	0	<0.1	0	<0.1
d.c. Stark	−4	4	−3.5	2.1
Background gas collisions	0	0.07	0	0.6
AOM phase chirp	−7	20	0.6	0.4
Second-order Doppler	0	<0.1	0	<0.1
Servo error	1	4	0.4	0.6
Totals	−5,704	53	−5,921.2	6.4

Shifts and uncertainties are given in fractional frequency units multiplied by 10^{-18}. Uncertainties are quoted as 1σ standard errors. They are determined with the square root of the quadrature sum of the systematic error and statistical error, with the latter quantity inflated by $\sqrt{\chi^2_{\text{reduced}}}$. For SrI, the significant digit for each uncertainty ends at the 1×10^{-18} level; for SrII, the significant digit is extended to the 1×10^{-19} level. See the text and Methods for a detailed discussion of all these systematic uncertainties, including the hyperpolarizability effect of the lattice Stark shift.

in situ silicon diode temperature sensors (with calibrations traceable to the National Institute of Standards and Technology (NIST)) near the atoms to measure their radiative heat environment (Fig. 2a). The sensors were affixed to separate glass tubes (Fig. 2a), which prevented parasitic heat conduction from the chamber to the sensors by providing insulation and radiative dissipation of conductive heat. To improve the radiative coupling, the surfaces of the sensors were coated with high absorptivity, ultrahigh-vacuum-compatible paint. One sensor was mounted 2.54 cm away from the atoms and provided real-time temperature monitoring during clock operation. The second sensor was affixed to an in-vacuum translator, allowing us to map the temperature gradients near the lattice-confined atoms (inset to Fig. 2c). During clock operations the mechanical translator was retracted to avoid interference with atoms (Fig. 2b). Systematic errors in both the readout of the sensors and their ability to determine the actual thermal distribution at the position of the atoms resulted in an overall uncertainty of 26.7 mK for the stated BBR temperature. Table 2 lists the sources of uncertainties for this temperature evaluation.

The atoms are influenced not only by the total integrated power of the BBR inside the chamber, known as the BBR static correction, but also the frequency-weighted spectrum of the radiation inside the chamber, known as the BBR dynamic correction. We constructed a ray-tracing model of our chamber to estimate the influence of temperature gradients throughout the vacuum chamber[24,25]. The model predicts the error incurred in the BBR dynamic correction by calculating the deviation from a perfect BBR spectrum for the temperature read out by the sensor[26] (see Methods). A perfect BBR environment corresponds to a spatially uniform temperature; deviations from such an environment cause a temperature gradient inside the chamber. As shown in Fig. 2c, components that couple strongly to the sensor, such as the large viewports, would need to deviate in temperature from the rest of the chamber by a significant amount (more than 10 K) for this error to reach the 1×10^{-18} level. Furthermore, within our BBR shielding box with small temperature gradients, the dominant emissivity-weighted solid angle of the vacuum viewports made the model's predictions for the dynamic BBR correction insensitive to the exact emissivity values. We ensured that the BBR shielding box is fully sealed from the outside environment, 'forbidding' the atoms to 'view' any highly emissive object with a temperature differing from the inside ambient temperature. This BBR shielding box also allowed the clock vacuum chamber to be insulated from room-temperature variations, because it reaches an equilibrium temperature of 301 K after two hours of clock operation.

Most systematics listed in Table 1 are rapidly measured through self-comparison with digital lock-in[6,27] (see Methods). Both SrI and SrII measure their systematics by modulating a particular physical parameter

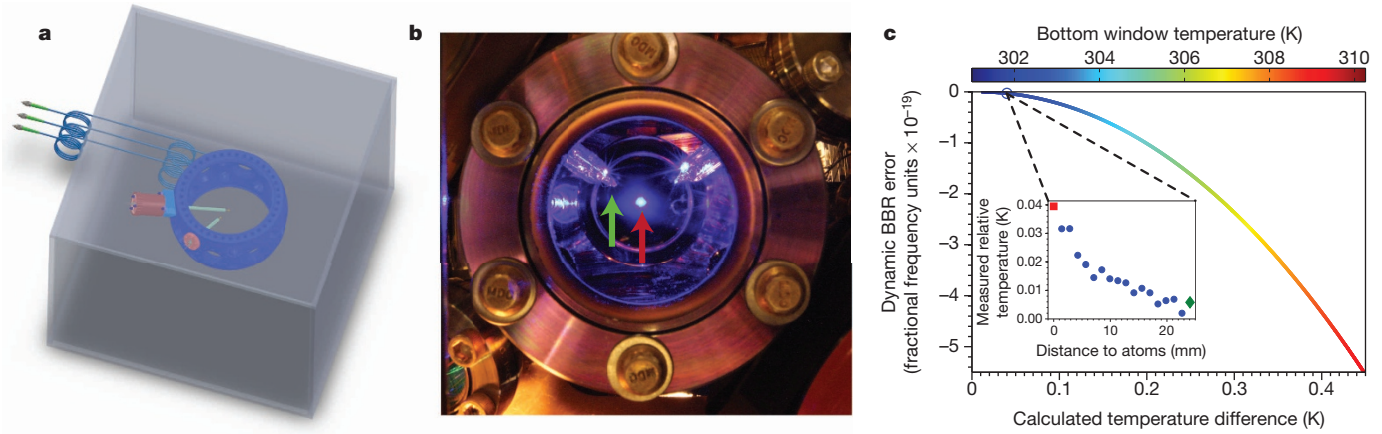

Figure 2 | Characterizing BBR effects on the $^1S_0$–$^3P_0$ transition. **a**, A three-dimensional model of the clock vacuum chamber. The sensor mounted on an in-vacuum translator is depicted in its fully extended mode of operation. The entire clock chamber resides inside a BBR shielding box with an equilibrium temperature of 301 K. **b**, A photograph of the two glass tubes surrounding the trapped ^{87}Sr atoms (red arrow). The movable sensor (green arrow) has been retracted for its normal operation. **c**, The error inherent in assuming a perfect BBR spectrum inside the vacuum chamber, based on a measurement of total BBR radiated power. Modelling all components of the chamber as 301 K and varying the bottom window temperature (shown in the top horizontal axis) shows that measuring the total radiative power is sufficient for our quoted BBR systematic uncertainty. The bottom horizontal axis displays the temperature difference between the atoms and the retracted sensor. The inset is a typical measured temperature difference inside the vacuum chamber referenced to the temperature of the retracted movable sensor at the beginning of the measurement. Green diamond, retracted position; red square, atomic position.

every two experimental cycles, with the clock laser serving as a stable reference with which to measure the related frequency shifts. For example, the atomic density shift was measured to high precision with this method. The SrII system is designed to reach a density shift uncertainty below 1×10^{-18} by using large lattice trapping volumes. To accommodate this, we used a Fabry–Perot buildup cavity to achieve a sufficiently deep lattice. This trap design increases the number of atoms loaded into the lattice at a decreased atomic density, allowing SrII to measure an already-reduced density shift to very high precision. Details of the SrI and SrII optical lattice trap geometries can be found in ref. 6 and in Methods.

Frequency shifts induced by the optical lattice potential must be understood and controlled at an extremely high level of precision, especially for optical lattices that trap weakly against gravity[28]. We used a variety of methods to stabilize the lattice scalar, vector and tensor Stark shifts. An 813-nm continuous-wave Ti:sapphire laser was used to create the lattice light for SrII. The clean spectrum of the solid-state laser has the advantage over a semiconductor tapered-amplifier-based lattice, where spontaneous noise pedestals might cause additional frequency shifts[9]. For SrI, we used a tapered-amplifier system, but we refined the output spectrum with a narrow-band interference filter and an optical filter cavity. To deal with potential residual shifts due to the tapered-amplifier noise pedestals, we regularly calibrated the lattice Stark shift for SrI. Both clocks stabilize their lattice laser frequencies to a Cs clock via a self-referenced Yb fibre comb, and their trapping light intensities were stabilized after being delivered to the atoms. The lattice vector shift was cancelled by alternately interrogating the $+9/2$ and $-9/2$ stretched nuclear spin states of the atom on successive experimental cycles, in addition to the use of linearly polarized lattice light[8,28]. This interrogation sequence also allowed cancellation of the first-order Zeeman shift. Rather than trying to separate the scalar and tensor shifts artificially, we treat them as a single effect in our measurement of the a.c. Stark shift[28]. (In reference to alternating (or direct) current, a.c. (or d.c.) is used to denote oscillatory (or static) fields and their effects.) We further minimized the tensor shift's sensitivity to the magnetic bias field B by setting the lattice polarization and the direction of B to be parallel. When modulating the intensity of the lattice, we did not identify any lattice shifts that are nonlinear in lattice intensity. Specifically, we eliminated systematic biases arising from differential atomic interaction shifts and optical spectrum shifts from the a.c. Stark effect. A Fisher test performed for various model shifts on an extensive set of data (shown in Fig. 3a) demonstrated that the lattice shift is consistent only with a linear model to within 1σ uncertainty (see Methods).

Table 2 | Uncertainties for the in-vacuum silicon diode thermometer

Corrections	ΔT (mK)	σ_T (mK)
Calibration (including self-heating)	0	16
Residual conduction	0	0.7
Temperature gradient	40	20
Lead resistance	7.7	1.5
Lattice light heating	−15	7.5
Totals	32.7	26.7

All uncertainties are quoted as 1σ standard errors. The absolute calibration of the silicon diode sensor (including the self-heating effect) was performed by the vendor (Lake Shore Cryotronics) and the calibration is traceable to the NIST blackbody radiation standard. We have evaluated corrections and their uncertainties for the operation of the sensors in our vacuum chamber, including the residual conduction by the mount, extra lead resistance and lattice light heating.

For SrII we also took extra care to minimize fluctuations in the magnetic-field-related lattice Stark effect and the second-order Zeeman shift[28]. To stabilize the magnetic field for our clock over long operational periods, we used the atoms themselves as a collocated magnetometer for the clock. Every two minutes during the clock operation, the computer-based frequency locking program was paused to interrogate unpolarized atomic samples under zero applied magnetic field. A drift in the background magnetic field resulted in a reduced excitation for the peak of an unpolarized line, because all ten nuclear spin states will experience different Zeeman shifts. Every time the magnetic field servo was activated, the program automatically dithered each pair of magnetic field compensation coils (along three orthogonal spatial directions) and optimized the current for each pair of coils. As shown in Fig. 3b, the magnetometer-based feedback loop not only keeps the field direction constant throughout the clock operation, but also automatically nulls the background field without an operator's intervention. For SrI, this procedure is unnecessary owing to its more stable magnetic field environment.

To push the systematic evaluation to the 10^{-18} level, we also needed to evaluate the d.c. electric-field-induced Stark effect, a frequency shift mechanism caused by patch charges immobilized in the vacuum chamber's fused silica viewports[29]. A pair of disk-shaped electrodes was placed near the two largest viewports in the system (separated along the vertical direction) and shifts were recorded as the electrode polarity was switched. Differences between the frequency shifts induced by oppositely charged electrodes indicate the presence of stray background electric fields, as shown in Fig. 3c. On first measuring the d.c. Stark

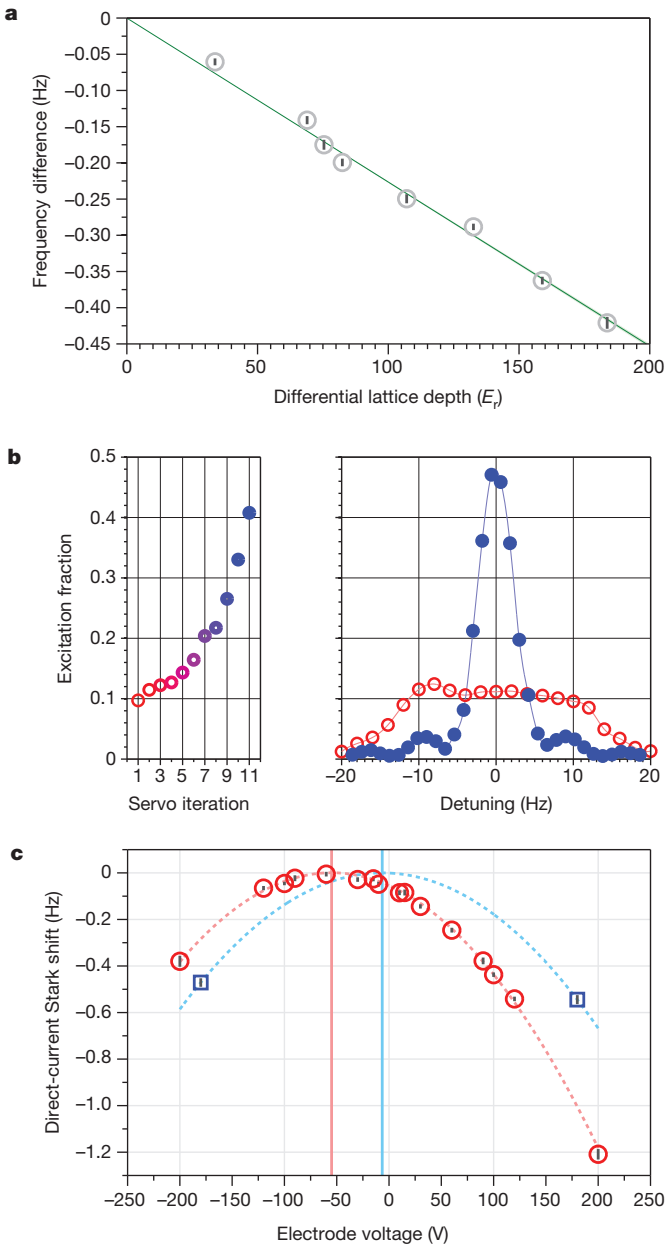

Figure 3 | Examples of systematic evaluations. a, To determine the lattice a.c. Stark effect accurately, a variety of lattice depths were used. This effect is depicted as a function of the differential lattice depth with binning chosen for figure clarity (average bin size 68 min, corresponding to an average of 1,600 points). Within our measurement precision, the best fit is a linear model. Grey circles denote mean frequency shifts and small solid black lines represent the 1σ standard errors inflated by the square root of the reduced chi-squared. The solid green line is a linear model and the light green patch represents the 1σ standard error for this model. **b**, Using the atomic cloud as a collocated magnetometer, a residual non-zero magnetic field is inferred via the peak excitation of an unpolarized Rabi lineshape. The left panel shows the servo action of zeroing the residual magnetic field. The right panel shows a clock transition lineshape for an unstabilized magnetic field (red open circles) and an improved lineshape under the stabilized magnetic field (blue filled circles). The red and blue solid lines are simply guides for the eye. **c**, Measurements of d.c. electric-field-induced Stark shift show a quadratic behaviour. The red circles show that a residual shift due to the stray d.c. field was -1.3×10^{-16}. The blue squares show a greatly reduced shift after purging the vacuum chamber with N_2 gas. Dashed lines show a quadratic fit to the data. Solid black lines represent the 1σ standard errors inflated by the square root of the reduced chi-squared. Solid red and blue vertical lines show the locations of zero net electric field.

effect on SrII, a residual, stable -1.3×10^{-16} shift was discovered. However, when the vacuum chamber was filled with clean nitrogen and then re-evacuated, we reduced the measurable d.c. Stark effect to $-1.6(1.0) \times 10^{-18}$. To complete the full evaluation of the d.c. Stark effect, we performed similar measurements along the horizontal direction and determined its effect at $-1.9(1.9) \times 10^{-18}$.

The outlook for optical lattice clocks is bright. We note that this is only the first systematic evaluation of a lattice clock enabled by the new generation of stable lasers, which led to clock stability near the quantum projection noise limit for 1,000 atoms. As laser stability continues to improve[30], Sr and other lattice clocks will increase their quantum-projection-noise-limited precision with larger numbers of atoms. Along with great advances in stability, the systematic uncertainty for such clocks will rapidly decrease owing to much reduced measurement times. Hence, the stability and total uncertainty of future lattice clocks will advance in lockstep. The techniques demonstrated here will allow for clock stability and total uncertainty below 1×10^{-18}. Such clocks will in turn push forward a broad range of quantum sensor technologies and facilitate a variety of fundamental physics tests.

METHODS SUMMARY

For both clocks, a few thousand ^{87}Sr atoms are laser cooled to around 3 μK and trapped in one-dimensional optical lattices near the magic wavelength (813 nm), with trap depths ranging from $40E_r$ to $300E_r$ (where E_r is the photon recoil energy). A thermal-noise-limited laser with a short-term stability of 1×10^{-16} (from 1 s to 1,000 s) interrogates the $^1S_0$–$^3P_0$ clock transition with Rabi spectroscopy for 160 ms. The clock comparison is normally operated in an asynchronous interrogation mode, where the two clock probe pulses are purposely non-overlapping in time[6]. Two independent acousto-optic modulators (AOMs) are used to correct the laser frequency to the SrI and SrII clock transitions. State detection of atomic ensembles is a destructive measurement that requires the repetition of the experimental cycle every 1.3 s. After each cycle, the frequency corrections, atom numbers and environmental temperatures for both systems are recorded and time stamped. For evaluation of the systematic uncertainty of the clock frequency, we focus on a few dominating effects such as the blackbody radiation, atomic interaction, lattice Stark shift and magnetic field, as well as a range of other sources of uncertainties such as the d.c. Stark shift, the clock laser a.c. Stark shift, line pulling and lattice tunnelling effects, AOM phase chirp, the second-order Doppler effect, background gas collisions and atomic servo errors. All experimentally measured quantities are treated with rigorous statistical analysis. Long time records of data are binned into various sizes of time windows, producing means and standard deviations of these bins along with the reduced chi-squared, $\sqrt{\chi^2_{\mathrm{reduced}}}$. When $\sqrt{\chi^2_{\mathrm{reduced}}} > 1$, indicating overscatter in data, the smaller bins' standard deviations are scaled up to bring $\sqrt{\chi^2_{\mathrm{reduced}}}$ to 1, and the analysis to determine the systematic is repeated.

Online Content Any additional Methods, Extended Data display items and Source Data are available in the online version of the paper; references unique to these sections appear only in the online paper.

Received 2 September; accepted 4 December 2013.
Published online 22 January 2014.

1. Wineland, D. J. Nobel lecture: Superposition, entanglement, and raising Schrödinger's cat. *Rev. Mod. Phys.* **85,** 1103–1114 (2013).
2. Haroche, S. Nobel lecture: Controlling photons in a box and exploring the quantum to classical boundary. *Rev. Mod. Phys.* **85,** 1083–1102 (2013).
3. Chou, C. W., Hume, D. B., Koelemeij, J. C. J., Wineland, D. J. & Rosenband, T. Frequency comparison of two high-accuracy Al^+ optical clocks. *Phys. Rev. Lett.* **104,** 070802 (2010).
4. Huntemann, N. *et al.* High-accuracy optical clock based on the octupole transition in $^{171}Yb^+$. *Phys. Rev. Lett.* **108,** 090801 (2012).
5. Madej, A. A., Dubé, P., Zhou, Z., Bernard, J. E. & Gertsvolf, M. $^{88}Sr^+$ 445-THz single-ion reference at the 10^{-17} level via control and cancellation of systematic uncertainties and its measurement against the SI second. *Phys. Rev. Lett.* **109,** 203002 (2012).
6. Nicholson, T. L. *et al.* Comparison of two independent Sr optical clocks with 1×10^{-17} stability at 10^3s. *Phys. Rev. Lett.* **109,** 230801 (2012).
7. Hinkley, N. *et al.* An atomic clock with 10^{-18} instability. *Science* **341,** 1215–1218 (2013).
8. Ludlow, A. D. *et al.* Lattice clock at 1 x 10^{-16} fractional uncertainty by remote optical evaluation with a Ca clock. *Science* **319,** 1805–1808 (2008).

9. Le Targat, R. *et al.* Experimental realization of an optical second with strontium lattice clocks. *Nature Commun.* **4,** 2109, http://dx.doi.org/10.1038/ncomms3109 (2013).
10. Falke, S. *et al.* The ^{87}Sr optical frequency standard at PTB. *Metrologia* **48,** 399–407 (2011).
11. Bordé, C. J. Base units of the SI, fundamental constants and modern quantum physics. *Phil. Trans. R. Soc. A* **363,** 2177–2201 (2005).
12. Rosenband, T. *et al.* Frequency ratio of Al^+ and Hg^+ single-ion optical clocks; metrology at the 17th decimal place. *Science* **319,** 1808–1812 (2008).
13. Chou, C. W., Hume, D. B., Rosenband, T. & Wineland, D. J. Optical clocks and relativity. *Science* **329,** 1630–1633 (2010).
14. Martin, M. J. *et al.* A quantum many-body spin system in an optical lattice clock. *Science* **341,** 632–636 (2013).
15. Ye, J., Kimble, H. J. & Katori, H. Quantum state engineering and precision metrology using state-insensitive light traps. *Science* **320,** 1734–1738 (2008).
16. Takamoto, M., Hong, F.-L., Higashi, R. & Katori, H. An optical lattice clock. *Nature* **435,** 321–324 (2005).
17. Kessler, T. *et al.* A sub-40-mHz-linewidth laser based on a silicon single-crystal optical cavity. *Nature Photon.* **6,** 687–692 (2012).
18. Bishof, M., Zhang, X., Martin, M. J. & Ye, J. Optical spectrum analyzer with quantum limited noise floor. *Phys. Rev. Lett.* **111,** 093604 (2013).
19. Campbell, G. K. *et al.* Probing interactions between ultracold fermions. *Science* **324,** 360–363 (2009).
20. Swallows, M. D. *et al.* Suppression of collisional shifts in a strongly interacting lattice clock. *Science* **331,** 1043–1046 (2011).
21. Lemke, N. D. *et al.* p-Wave cold collisions in an optical lattice clock. *Phys. Rev. Lett.* **107,** 103902 (2011).
22. Middelmann, T., Falke, S., Lisdat, C. & Sterr, U. High accuracy correction of blackbody radiation shift in an optical lattice clock. *Phys. Rev. Lett.* **109,** 263004 (2012).
23. Boyd, M. M. *et al.* Optical atomic coherence at the 1-second time scale. *Science* **314,** 1430–1433 (2006).
24. Chandos, R. J. & Chandos, R. E. Radiometric properties of isothermal, diffuse wall cavity sources. *Appl. Opt.* **13,** 2142–2152 (1974).
25. Yasuda, M. & Katori, H. Lifetime measurement of the $^3P_2$ metastable state of strontium atoms. *Phys. Rev. Lett.* **92,** 153004 (2004).
26. Middelmann, T. *et al.* Tackling the blackbody shift in a strontium optical lattice clock. *IEEE Trans. Instrum. Meas.* **60,** 2550–2557 (2011).
27. Boyd, M. *et al.* ^{87}Sr lattice clock with inaccuracy below 10^{-15}. *Phys. Rev. Lett.* **98,** 083002 (2007).
28. Westergaard, P. G. *et al.* Lattice-induced frequency shifts in Sr optical lattice clocks at the 10^{-17} level. *Phys. Rev. Lett.* **106,** 210801 (2011).
29. Lodewyck, J., Zawada, M., Lorini, L., Gurov, M. & Lemonde, P. Observation and cancellation of a perturbing dc stark shift in strontium optical lattice clocks. *IEEE Trans. Ultrason. Ferroelectr. Freq. Control* **59,** 411–415 (2012).
30. Cole, G. D., Zhang, W., Martin, M. J., Ye, J. & Aspelmeyer, M. Tenfold reduction of Brownian noise in high-reflectivity optical coatings. *Nature Photon.* **7,** 644–650 (2013).

Acknowledgements We thank M. Martin, M. Swallows, E. Arimondo, J. L. Hall, T. Pfau, and W. D. Phillips for discussions and H. Green for technical assistance. This research is supported by the National Institute of Standards and Technology, the Defense Advanced Research Projects Agency's QuASAR Program, and the NSF PFC. M.B. acknowledges support from the National Defense Science and Engineering Graduate fellowship programme. S.L.C. and M.B. acknowledge support from the NSF Graduate Fellowship. Any mention of commercial products does not constitute an endorsement by NIST.

Author Contributions B.J.B., T.L.N., J.R.W., S.L.C., M.B., X.Z., W.Z., S.L.B. and J.Y. conceived, designed and carried out the experiments mentioned in this manuscript. All authors discussed the results and contributed to the manuscript.

Author Information Reprints and permissions information is available at www.nature.com/reprints. The authors declare no competing financial interests. Readers are welcome to comment on the online version of the paper. Correspondence and requests for materials should be addressed to J.Y. (ye@jila.colorado.edu).

METHODS

Atomic sample preparation. For both clocks, up to a few thousand ^{87}Sr atoms are laser cooled to a few microkelvin and trapped in one-dimensional optical lattices near the magic wavelength (813 nm), with trap depths ranging from $40E_r$ to $300E_r$. Here E_r is the photon recoil energy. A thermal-noise-limited laser with a short-term stability of 1×10^{-16} (from 1 s to 1,000 s) interrogates the $^1S_0$–$^3P_0$ clock transition with Rabi spectroscopy over a 160-ms probe time. We allow a sufficient time for transient perturbations in the system to decay before we interrogate the clock transition. We normally operate the clock comparison in an asynchronous interrogation mode, where the two clock probe pulses are purposely non-overlapping in time[6]. Two independent frequency shifters (acousto-optic modulators (AOMs)) are used to correct the laser frequency to the SrI and SrII clock transitions. State detection of both atomic ensembles is a destructive measurement that requires the repetition of the experimental cycle every 1.3 s. After each cycle, the frequency corrections, atom numbers, and environmental temperatures for both systems are recorded and time stamped for comparison and post-processing.

Statistical methods for data analysis. For all systematic measurements, residual non-white noise introduces overscatter in the data. Following our previously reported procedure[20], the data are first binned into smaller chunks, the means and standard deviations of these bins are determined, and a reduced chi-squared, $\sqrt{\chi^2_{\text{reduced}}}$, is obtained. In instances where $\sqrt{\chi^2_{\text{reduced}}} > 1$, indicating overscatter in the data, the smaller bins' standard deviations are inflated to bring $\sqrt{\chi^2_{\text{reduced}}}$ to 1, and the analysis to determine the systematic is repeated. This conservative approach is applied to all measurements in this Letter unless otherwise noted.

Previously, the most comprehensive systematic evaluations of optical lattice clocks with total systematic uncertainty better than that of Cs were reported in refs 8–10 and 31. During the production of this manuscript, another systematic evaluation of Sr from the Physikalisch-Technische Bundesanstalt group has been released[32]. Below, we provide a detailed discussion of the systematics we evaluated in this work.

Blackbody radiation shifts. The blackbody radiation shift is determined by $\Delta\nu_{\text{BBR}} = -2.13023(T/300)^4 - 0.1484(T/300)^6$, where T is the temperature in K and $\Delta\nu_{\text{BBR}}$ has units of Hz. The T^4 term is known as the static shift, and the T^6 term is called the dynamic shift. To ascertain the radiative temperature experienced by the atoms, silicon diode temperature sensors were installed in SrII. Silicon diode sensors are used for their ease of calibration (because their forward voltage drop is linear in temperature) and their suitability for vacuum baking[33]. We investigate the thermalization of the probes by modelling their heat transfer. For the small thermal gradients measured around our chamber, the sensors give a good measurement of the integrated BBR spectrum, which is proportional to the static BBR shift experienced by the atoms.

The dynamic shift, which depends on the frequency-weighted spectrum of radiation experienced by the atoms, is calculated using the temperature read out by the sensor. The T^6 coefficient associated with this shift was chosen to be a simple mean between the two most recent publications and the uncertainty in this coefficient was chosen to be their difference[22,34]. This coefficient uncertainty is the dominant BBR uncertainty. To understand the error we accrue by calculating the dynamic shift with the sensor reading, a ray-tracing model of our chamber was constructed. Refraining from using a Monte Carlo population of rays, we used Hammersley boundary points to construct the ray population in a controlled, repeatable and processor-efficient manner. Effective emissivity-weighted solid angles are then tabulated according to whatever position inside the main chamber the end user requires. By keeping track of the approximate blackbody radiation spectrum at any point in the chamber and using the relevant Einstein A coefficients of Sr in ref. 22, the error associated with assuming a perfect BBR spectrum was determined. The model's results, as seen in Fig. 2c, show that this error is well below our quoted systematic uncertainty for BBR under small temperature variations around our chamber.

Within our BBR shielding box with small temperature gradients, the dominant emissivity-weighted solid angle of the vacuum viewports makes the model's predictions for the dynamic BBR correction insensitive to the exact emissivity values. For example, for small temperature differentials (3 K) across our chamber, the emissivity of the metal would need to change by a factor of 20 to introduce a 1×10^{-18} error into the model's predictions.

However, much hotter components that couple more strongly to the atoms, such as the heated Zeeman slower window, introduce a larger error in the deviation from a perfect BBR spectrum. For the systematic uncertainty evaluation, the operation of the Sr optical lattice clock can be performed without heating the Zeeman slower window for a limited amount of time. Even with the Zeeman slower window heated, its contribution to total uncertainty is below 1.2×10^{-18}. For future experiments that require total uncertainty below 1×10^{-18}, we can simply add mechanical shutters that obscure the atoms' view of all hot elements in the system. SrI's temperature is a simple weighted mean, based on a set of temperature measurements made at various points on the chamber. The weights for this mean are derived from the emissivity-weighted solid angles the atoms experience from various components. We conservatively quote the full range of temperature across the SrI chamber (0.7 K) as the SrI temperature uncertainty.

Atomic density shifts. For both SrI and SrII, the atomic density shift is measured via self-comparison by modulating the lattice trapped atom number during subsequent measurements of the line centre. The fast modulation timescale makes these measurements immune to long-term atom number drifts. Extrapolation of the density shift from changes in atomic density due to changes in the lattice trapping potential is used only when trap frequencies have changed by less than 10%. Any additional error from this extrapolation is included in the final quoted uncertainty.

Magnetic field effects. The first-order Zeeman shifts are cancelled by alternately interrogating opposite nuclear spin stretched states. After each line centre acquisition of the clock laser, the quoted Sr frequency is the running average between the two previous measurements. Key to the efficacy of this scheme is that changes in the magnetic field over two line centre acquisitions are either negligible or averaged away. The residual first-order Zeeman shift is calculated by examining the overall drift of the magnetic field splitting between the two stretched nuclear spin states, and extrapolating the inherent shift this drift would induce.

The second-order Zeeman shifts, caused by the presence of an applied bias and a residual magnetic field during the clock interrogation sequence, are subtracted off point by point. The determination of the second-order Zeeman shift coefficient is made via a fast modulation experiment whereby four digital locks are modulated in sequence: two locks at a high magnetic field, one for a measurement of each stretched spin component, and two locks at a low magnetic field. This experiment was performed for stretched states' splitting ranging from 300 Hz to 1,200 Hz. To fit this data, a quadratic function, cS^2, was used. Here c was found to be $-0.248(2) \times 10^{-6}\,\text{Hz}^{-1}$, and S is the measured stretched state splitting in Hz. Extra care was taken to ensure that modulation of the applied bias field did not cause any rotation of the polarization axis, which would induce an unwanted differential lattice tensor shift. The second-order Zeeman shift uncertainty is quoted for a 500-Hz splitting between the $m_f = \pm 9/2$ stretched states, which allows for a relatively strong bias magnetic field (about 50 μT) to be applied to the atoms during clock operation.

During the course of the previous measurement, instabilities in the magnetic field environment of SrII were discovered. Active control of the magnetic field was implemented to combat this. As detailed in the main text, the peak excitation of an unpolarized line is used as a measure of the residual magnetic field in the system. Once the clock has entered into the servo routine, it takes three peak excitation measurements for each coil at different currents ($I_0 - \Delta I$, I_0, $I_0 + \Delta I$, where I_0 is the current of the previous iteration and ΔI is a small trial step). In situations where the residual field is far from zero, the software steps the current by a fixed amount in the direction indicated by the increasing excitation. When the field is near zero, a parabola was fitted between the three measurements and the current was stepped to the fitted value filtered via a low-pass finite impulse response filter. On stopping the servo routine and measuring the unpolarized line, the residual magnetic field wander was measured to be less than 0.3 μT.

Lattice Stark effects. To achieve the low uncertainties reported for SrII, a variety of new techniques were used to minimize any systematic errors in the measurement of the lattice stark effects. The intensity servos were implemented with a liquid-crystal waveplate for SrI and an acousto-optic modulator for SrII. Trap frequency measurements were performed at each measured a.c. Stark point via a high-resolution sideband scan. As explained in ref. 35, radial motion only brings the sidebands closer to the carrier, so the true longitudinal sideband frequency is found by looking at the farthest edge of the blue sideband. This edge corresponds to the contributions of atoms that are distributed at the centre of the Gaussian profile for the lattice beam. A tangent line was fitted to the inflection point of the Lorentzian, and then the Lorentzian centre frequency could be extrapolated from the tangent x-intercept and the Lorentzian linewidth determined by the Fourier-limited linewidth of the clock laser scan. A scan of the carrier was taken simultaneously with these high-resolution sideband scans, and a fit to the carrier was used to determine the Lorentzian linewidth. Once the longitudinal trap frequency was determined, the trap depth could be extracted using the procedures outlined in ref. 35. Alternating between four atomic servos, with the magnetic field control activated, we measured differential shifts between a variety of high and low lattice depths from $87E_r$ to $300E_r$ for the SrII apparatus. To minimize systematic uncertainties caused by differential atomic density shifts, both high and low lattice depths were operated with an absolute density shift below 1×10^{-17}. Atomic interaction shifts follow a power-law behaviour in the trap frequency, and must be taken into account especially at very high lattice depths. Atom numbers were chosen to provide similar density shifts for both high and low lattice depths. Furthermore, individual measurements for particular values of lattice depth difference were performed at 1×10^{-17} statistical uncertainty. Many measurements at different lattice depths were needed to achieve the low uncertainty reported here (see Fig. 3a). Raw measurement data are binned in sets of 30 to 75 points per bin

according to the procedure outlined in the 'Statistical methods for data analysis' section. To decrease the sensitivity to bin choice, the final uncertainties for the fit parameter are simple means of the fit parameter errors determined for all bin sizes. Model fits for both a hyperpolarizability and an E2/M1 contribution to the measured stark shift revealed no statistically significant contribution, based on a Fisher test with a 1σ threshold. Even at this measurement precision, the small magnitude of these shifts allowed their contributions to be included in the linear fit. Our fitted hyperpolarizability, 0.48(47) $\mu Hz/E_r^2$, is not inconsistent with previously reported coefficients[9] of 0.45(10) $\mu Hz/E_r^2$. However, our data, as shown by the Fisher test, support a linear fit only. We thus list only a single overall systematic uncertainty for the lattice a.c. Stark shift, treating the entire data set in the most statistically consistent manner. We note that using a prior reported hyperpolarizability coefficient[9], our overall a.c. Stark uncertainty would change only slightly from 3.7×10^{-18} to 4.1×10^{-18}. However, in that previous measurement, to gain a very large lever arm for the measurement of the hyperpolarizability, very high ($5{,}000E_r$) lattice depths were used[9], but the atomic density effects in such tight traps were not considered. In summary, although our data are not inconsistent with the hyperpolarizability measurements previously reported[9], this work is not an independent verification of the previous measurement. Our data alone do not support a statistically significant nonlinearity, and the extracted hyperpolarizability would have a higher uncertainty than the previous measurement.

Although, to first order, lattice vector shifts are cancelled by alternately measuring opposite nuclear spin stretched states, a residual lattice vector shift can cause systematic shifts due to its convolution with the second-order Zeeman shift. A lattice vector shift will cause an overall widening of the shift between opposite nuclear spin states, mimicking a magnetic field. As a conservative estimate, we included the effect of a 100-mHz residual lattice vector splitting. To calculate how this will affect the uncertainty related to the second-order Zeeman effect, we included this 100 mHz as an error to S, as defined in the 'Magnetic field effects' section.

Miscellaneous shifts. Shifts from background gas collisions were estimated using the methods described in ref. 36. Differential C_6 coefficients for the Sr $^1S_0$ and $^3P_0$ states[37] for their resonant dipole interactions were scaled to the Cs ground-state–ground-state C_6 coefficients. By far the largest residual gas in our ultrahigh-vacuum, oven-loaded system is hydrogen. Both the Sr $^1S_0$-H_2 C_6 coefficient and the Sr $^3P_0$-H_2 C_6 coefficient were then estimated by scaling with respect to the non-resonant dipole Cs–H_2 C_6 coefficient. Atomic trapping lifetimes of about 1 s (SrII) and about 8 s (SrI), average excitations during the detuned Rabi pulse and interrogation times of 160 ms were combined to estimate the background gas collisional shift uncertainty. No shift correction is quoted, and we provide only an upper bound of this uncertainty.

Using the measured temperature of around 3 μK, we calculate an average total velocity of 3 cm s^{-1}. A Taylor expansion of the full relativistic Doppler shift has second-order terms from both longitudinal and transverse motion. Overall, the second-order Doppler effect results in a fractional shift less than 10^{-20}.

Line pulling can be caused by a variety of effects. These effects include a slight ellipticity in the clock laser polarization, imperfect optical pumping (<5% population in neighbouring nuclear spin states), and clock-laser-induced tunnelling (no signal was visible for tunnelling-induced sidebands). They can be modelled as a deformation of a perfect Rabi lineshape. The spectral narrowness of the 5-Hz Fourier-limited linewidth with which all data was taken in this work greatly reduced the effect of any possible line pulling.

The only exception to taking data with spectrally narrow features was the investigation of the a.c. Stark shift induced by the clock laser itself. This systematic was evaluated by measuring the frequency difference between our clock transition interrogated with 50-ms and 200-ms π pulses using our fast modulation technique. For this measurement, the clock was run with our largest possible bias magnetic field to avoid any residual line pulling effects during the 50-ms clock interrogation. Including the errors in determining our π pulse exactly, we estimate a 1.3×10^{-18} uncertainty in the probe beam a.c. Stark shift for SrII's normal clock operation.

An AOM is used to scan the ^{87}Sr clock transition and to shape our laser pulse. When the clock pulse is switched on, phase transients originating from this AOM can cause a measured frequency shift. We compared light from a diffracted order of this AOM with the zeroth-order light using a digital phase detector. After we calibrated and removed the effect of the detector's phase transients from our data, the observed effects, when convolved with the sensitivity function of Rabi spectroscopy, resulted in a shift almost consistent with zero[38].

Servo error was determined by combining many hours of lock data and measuring whether there is a systematic bias to the in-loop error signal. Any bias measured was transformed to a frequency shift and uncertainty by modelling a perfect Rabi lineshape with the contrast and pulse area under which the data was taken. This allowed us to transform error signal bias to frequency shifts.

Frequency comparison. After the data had been post-processed by each individual strontium team, time-stamped and corrected frequencies were shared. Although the overall systematic uncertainty of the comparison is 5.4×10^{-17}, as a consistency check for the comparison a variety of methods were used to show the agreement of the two clocks within this confidence interval. A simple mean of all the data gives the difference between the two clocks to be -2.4×10^{-17}. Binning the data in small chunks, of approximately one minute per data point (as in the top panel of Fig. 1b) gives agreement of $-2.8(2) \times 10^{-17}$. The uncertainty on this number has been inflated by $\sqrt{\chi^2_{\mathrm{reduced}}}$, because $\sqrt{\chi^2_{\mathrm{reduced}}} = 3.5$ denotes overscatter in the data. Binning the data in 30-min chunks (as in the bottom panel of Fig. 1b) clearly shows that there are systematic fluctuations still present in the comparison, with $\sqrt{\chi^2_{\mathrm{reduced}}} = 10.5$ and an agreement of $-2.7(5) \times 10^{-17}$. Again, this uncertainty is inflated by $\sqrt{\chi^2_{\mathrm{reduced}}}$. The greater overscatter in the data at longer timescales is probably caused by imprecise knowledge of the BBR environment for SrI, which allows for fluctuations within the 1σ comparison uncertainty.

The final systematic uncertainty used in the comparison is quoted under the running conditions of the two strontium systems during the comparison, and not their final best achieved total uncertainties. Furthermore, the height difference (10 cm) between the two atomic clouds, resulting in a 1.0×10^{-17} gravitational redshift, was included in the comparison but was not relevant for Table 1.

31. Campbell, G. K. *et al.* The absolute frequency of the ^{87}Sr optical clock transition. *Metrologia* **45,** 539–548 (2008).
32. Falke, S. *et al.* A strontium lattice clock with 3×10^{-17} inaccuracy and its frequency. Preprint at http://arxiv.org/abs/1312.3419 (2013).
33. McNamara, A. G. Semiconductor diodes and transistors as electrical thermometers. *Rev. Sci. Instrum.* **33,** 330–333 (1962).
34. Safronova, M. S., Porsev, S. G., Safronova, U. I., Kozlov, M. G. & Clark, C. W. Blackbody-radiation shift in the Sr optical atomic clock. *Phys. Rev. A* **87,** 012509 (2013).
35. Blatt, S. *et al.* Rabi spectroscopy and excitation inhomogeneity in a 1D optical lattice. *Phys. Rev. A* **80,** 052703 (2009).
36. Gibble, K. Scattering of cold-atom coherences by hot atoms: frequency shifts from background-gas collisions. *Phys. Rev. Lett.* **110,** 180802 (2013).
37. Santra, R., Christ, K. & Greene, C. Properties of metastable alkaline-earth-metal atoms calculated using an accurate effective core potential. *Phys. Rev. A* **69,** 042510 (2004).
38. Falke, S., Misera, M., Sterr, U. & Lisdat, C. Delivering pulsed and phase stable light to atoms of an optical clock. *Appl. Phys. B* **107,** 301–311 (2012).